International Journal for Multidisciplinary Research (IJFMR)
E-ISSN: 2582-2160 ● Website: www.ijfmr.com ● Email: editor@ijfmr.com

Erbium Doped Strontium Hexaferrites Synthesis and Structural, Thermal, Magnetic, Optical Properties And Photocatalytic Application

A. Thippeswamy[1], C Mahendra Kumar [2], G. Krishnamurthy[3]

[1]Department of PG Studies in Industrial Chemistry, Government Arts and Science College, Karwar, Karnataka, India-581301

[2]Department of Biotechnology, Government Arts and Science College, Karwar, Karnataka, India-581301

[3]Department of PG Studies and Research in Chemistry and Industrial Chemistry, Sahyadri Science College (Constituent college) of Kuvempu University, Shivamogga, Karnataka, India -577203

ABSTRACT

$SrEr_xFe_{12-x}O_{19}$(x=0, 0.01, 0.05 and 0.09) nanoparticles were synthesized by auto-combustion method using urea as a fuel. The structural changes on substitution of erbium to M-type strontium hexaferrites have been evaluated by scanning electron microscope (SEM), FTIR, Energy dispersive X-ray spectroscopy (EDX) and Vibrating sample magnetometer (VSM), The thermogravimetric analysis (TGA) used to determine the stability and decomposition of nanoparticles. PXRD pattern confirms the crystalline size 30 nm indicates pure hexagonal crystal structure. The decrease of Hc 4939.8-5232.5(Oe) and Mr 15.84-19.31 (emu/g) Value with increasing erbium substitution and hard magnetization confirmed by VSM analysis. The optical band gap determined was 2.5 eV. The photodegradation of various dyes in the presence

of synthesised nanohexaferrites under the sun light showed that 4-nitroaniline undergo 98% effective degradation without loss of the catalyst.

Keywords: Self-propagation, photocatalytic properties, Vibrating sample magnetometer, TGA, hexagonal lattice and photocatalytic effect.

Introduction

Nanoparticle with particle size below 100 nm are important and has broad applications as permanent magnets and data storage devices, materials for absorbing electromagnetic radiations, high density magnetic recording, medical equipment macroscopic quantum tunneling (MQT), Site-specific drug delivery etc. [1]. There has been considerable intensity in using metal ferrites in photocatalysis. Among the ferrites, $CoFe_2O_4$ found to be stable structure and superior magnetic properties. This is due to two distinct tetrahedral and octahedral positions available for doping M^{2+} and M^{3+} ions. Thus, photochemical properties in them can be easily altered through doping and co-doping techniques [2]. In this respect, many novel doped nanoferrites synthesized and reported their properties. The substituted hexaferrrites also found to be have optimized photocatalytic properties which are classified in to six types based on their crystal structure. They are M, W, X, Y, Z and U type ferrites with the general formula $MFe_{12-x}O_{19}$ where M = Sr, Ba and Pb. Among these ferrites, the strontium doped ferrites make it more suitable for many optical and magnetic related applications due to its suitable size and charge [3-5]. Literature show that strontium doped ferrites used in finer recording media applications, low coercivity and high saturation magnetization values [6]. Further, variation in the amounts of both Sr^{2+} and Fe^{3+} alter the properties of doped ferrites. Substitution of Sr^{2+} ions by rare earth ions like La^{3+}, pr^{3+}, Nd^{3+}, Sm^{3+} etc., similarly, Fe^{3+} substitution Al^{3+}, La^{3+}, Gd^{3+}, Er^{3+}, Co^{2+}, Mn^{2+}, Nd^{3+}, Bi^{3+} etc., showed the properties that depend greatly on the (i) the composition, (ii) synthetic method and (iii) the calcination temperature. For example, M-type

hexagonal $SrFe_{12}O_{19}$ and $NdFe_{12}O_{19}$ synthesized by hydrothermal method which were sintered at 1200 ℃ in air showed increased coercivity without causing any significant changes in saturation magnetization and remanence even when the concentration of Sr^{2+} and Nd^{3+} in their respective ferrite is increased. In addition, M-type strontium hexaferrite is considered a synthetic magnetic material of great interest due to its excellent chemical stability, high Curie temperature, and corrosion resistance [7]. Erbium doping significant alters the magnetic and optical properties of nanoferrites it also has significant role in changing the crystal structure and lattice parameters. Erbium doping exhibits photoluminescence emission at 1534 nm and thus suitable in optical waveguides and amplifies [8]. There are a number of methods known to synthesize erbium doped nanomaterials. They are sol-gel, hydrothermal, Ball milling, Auto-combustion, micro-emulsion, green synthesis and co-precipitation methods. Among these the auto-combustion method at high temperature is very simple, having lower production cost with higher purity of the sample and obtain homogeneity in short time interval [9-11].

Water pollution is a major threat to Society. The main source of water pollution is industrial discharge. In recent decades due to urbanization and expansion of industries are the two critical issues. Major industrial sectors are textile, pharmaceutical, leather, cosmetic, beverages, cement, rubber, plastic, agriculture, paper industries and these industries are the primary sources of poisonous chemicals such as heavy metals, mineral acids, organic acids, bleaching agents, detergents, Inorganic particles, synthetic organic dyes and other residues which cause severe environmental pollutions [12] and is becoming a threat to water bodies and humans. Therefore, water treatment essentially required and it has been done by different methods, one of the best methods is ultraviolet purification, which involves the use of nanocomposites or semiconductor photocatalyst with tuneable bandgaps using TiO_2 and ZnO [13]. The first used catalyst for that purpose was titanium dioxide which has a strong potential for destroying the micro-organisms and other organic pollutants in the presence of UV light [14]. In addition, there are many TiO_2 based photocatalysts used widely due to its eco-friendly nature. Recently,

researchers have investigated that the strontium substituted ferrite nanoparticles also have potential optical applications [15]. Thus, a number of $SrFe_{12-x}O_{19}$ have been synthesized and evaluated their photocatalytic properties. Further, doping rare-earth elements to $SrFe_{12-x}O_{19}$ can further alter their photocatalytic properties.

Research in our laboratory focused on synthesis of rare-earth substituted hexaferrites by different methods by using different fuels and studied the photocatalytic properties [16]. In the present research work, we report here the synthesis of Er^{3+} substituted of $SrFe_{12-x}O_{19}$ (x=0, 0.01, 0.05 and 0.09) by auto-combustion method using urea as a fuel and studied structural, morphological, magnetic optical and photocatalytic degradation of different dyes.

Experimental

Material and Methods

The samples for the preparation $Er_xSrFe_{12-x}O_{19}$ nanoparticles i.e., all metal nitrates and organic fuels used were of analytical grade. The metal precursors used were Ferric nitrate nonohydrates, $Fe(NO_3)_39H_2O$(purity 99%), erbium nitrate hexahydrate, $Er(NO_3)_36H_2O$, strontium nitrate $Sr(NO_3)_3$, and urea (CH_4N_2O), purchased from Merck chemicals and Nice chemicals. The synthesized nanoparticles were characterized by Fourier transform infrared spectroscopy (FTIR) on a perkin Elmer spectrometer (Spectrum 2 USA), Phase identification via powder X-ray diffraction (XRD) which were obtained in 2θ angle in the range 20-80° with Philips diffractometer (BRUKER, d8 Advance, Germany) using CuKα radiations (λ=1.5406 Å). The sample morphologies and micro structure were observed by emission scanning electron microscopy (ESEM, JEOl/EO/JSM-639). The energy dispersive X-ray spectrum were recorded using (EDX) (CarlZeiss, Model: EVOLS15, Germany). Vibrating sample magnetometer (VSM; CREST, 20130523-01) was employed to characterize the magnetic properties at room temperature. The saturation magnetization (Ms), Coercivity (Hc) and remanence magnetization (Mr) obtained from Hysteresis loops. Thermo gravimetric analysis (TGA) and differential

scanning calorimetry (DSC) was carried out by using NETZSCH, STA 2000 at 1000 ℃, this provides information about phase change, exothermic and endothermic events.

Procedure

The nanocomposites, $SrEr_xFe_{12-x}O_{19}$ (SrM-HF's) (x=0, 0.01, 0.05 and 0.09) have been synthesized by Auto-combustion method. All metal nitrates used in appropriate ratio and urea was dissolved in a small amount of deionized water taken in a beaker which was stirred by a magnetic stirrer at room temperature to get homogeneous solution. The mixture was kept in a furnace and heated to 500°C for about four minutes then a large amount of gas (N_2O and CO_2) released and large amount of heat released by completing the whole reaction. The sintered fluffy powders was ground in an mortar with pestle and mixed with a binder polyvinyl pyrolidone (PVP) $(C_6H_9NO)_n$. The fluffy powders are compressed to dia 10 mm and a thickness of about 3 mm by loading a pressure of 8-106 kg/m^2 for 6 min. The pellets were sintered in a furnace at the temperature of 1200°C for 3h and then gradually cooled to room temperature. The experimental condition favourable for obtaining nanoparticles in the significant crystalline state.

Photocatalytic activity of the synthesized SrM-HF's was determined under solar light. The time taken for decomposition of different dye was measured. In each experiment, 0.05 g of SrM-HF's nanoparticles were added into 50 mL of dye solution with a concentration of 10 mg (1:1molar ratio). The suspension was magnetically stirred in the dark for 30 minutes to establish the adsorption/desorption equilibrium at room temperature, then the solution was directly irradiated under sunlight. After that samples were taken from the suspension and centrifuged to remove the SrM-HF's nanoparticles. The change in the concentration of each degraded solution was determined by UV–Vis spectrophotometer (Shimadzu, UV-1650 PL model) by measuring the absorbance in the range of 200–800 nm. Distilled water was used as the reference sample [17] and the percentage degradation of the aqueous dye solution was

calculated by the relation given below

$\eta = [(C_0 - C_t)/C_0] X100$ ……...(1)

Here, η is the degradation percentage (%), is the initial absorbance of the dye (mg/L); C_t is the absorbance of the dye at the selected time interval (mg/L) [18].

Results and Discussion

FTIR studies

FTIR spectroscopy used to find the presence of functional groups. In fig. 1, it is observed that two strong

characteristic absorption bands in the range 400-550 cm^{-1}, which are assigned to the intrinsic vibrations of tetrahedral and octahedral positions in the M-hexagonal lattice [19].

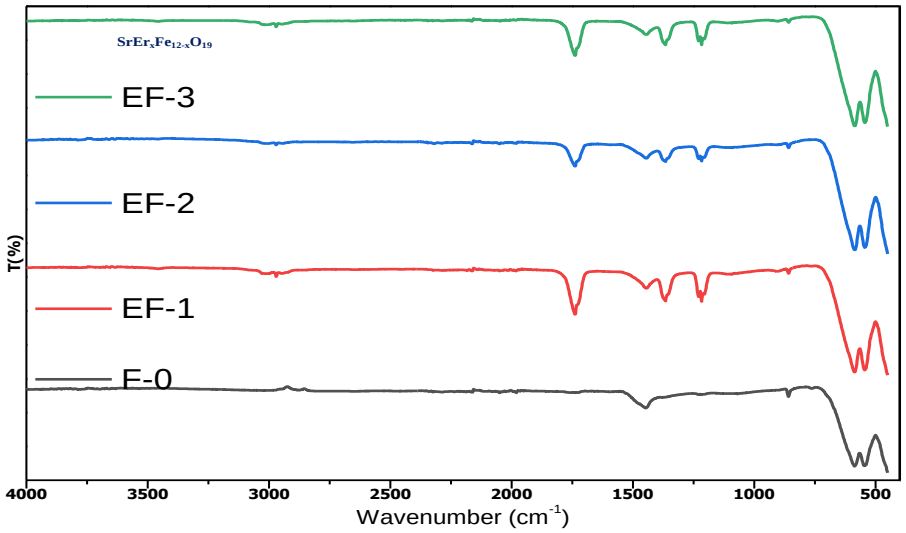

Fig. 1 FTIR spectra of $SrEr_xFe_{12-x}O_{19}$ (FO: x = 0.00, EF-1: x=0.01, EF-2: x=0.05 and EF-3: x= 0.09)

The absorption band in the region 454 and 591 cm^{-1} corresponds Fe-O stretching vibration [20]. These observations confirmed the formation of an M-type SrHF's structure. No absorption band appeared in the region 3200-3500 cm^{-1} indicates the absence of an OH group/moisture in the synthesized samples and confirming the completion of the reaction [21].

XRD analysis

The PXRD pattern of the $SrEr_xFe_{12-x}O_{19}$ (x=0, 0.01, 0.05 and 0.09) are showed in fig. 2. The peaks with h, k, l values of planes (110), (114), (200) and (203) matching with the JCPDS card number: **24-1207** for the hexagonal phase $SrFe_{12}O_{19}$ type.

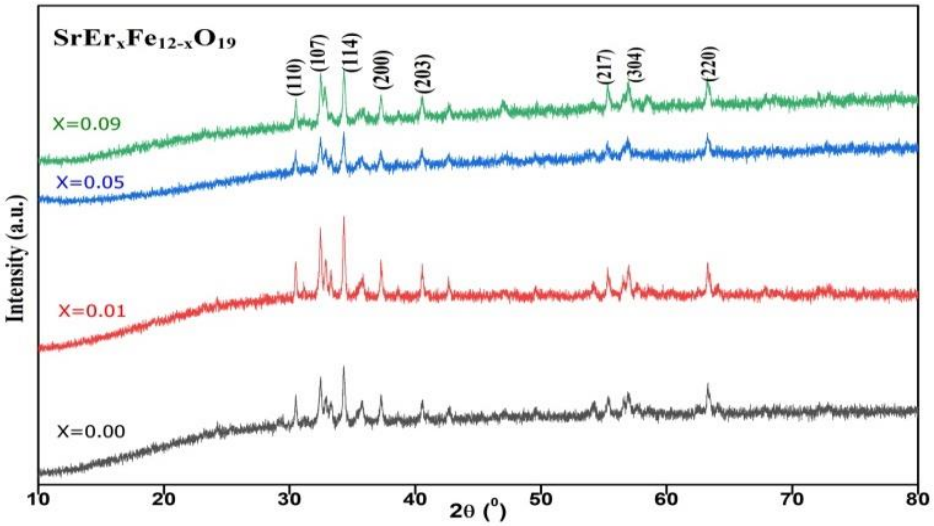

Fig. 2 XRD pattern of $SrEr_xFe_{12-x}O_{19}$ (FO: x = 0.00, EF-1: x=0.01, EF-2: x=0.05 and EF-3: x= 0.09) standard diffraction pattern JCPDS card number 24-1207

In addition, it was observed that the sample $SrEr_xFe_{12-x}O_{19}$ showed around 5% of phase of secondary erbium oxide (ICSD: 202518). The lattice parameter calculated using the relation,

$$\frac{1}{d^2\,\mathrm{hkl}} = \frac{4}{3}\left(\frac{h^2+hk+l^2}{a^2}\right) + \frac{l^2}{c^2} \qquad \text{..... (2)}$$

Where d_{hkl} is the crystal planes comparing the distance; a and c are the lattice parameters; and (hkl) are the Miller indices. XRD studies showed that the lattice parameter increased slightly from 0.5107 to 0.5729 cm^{-1}. The increase in lattice parameter with increasing the Er^{3+} ion concentration because of the substitution of larger ionic radius Sr^{+2} (0.112nm) with smaller ionic radius Er^{3+}ions (0.1098 nm) [22].

Table.1 Crystallite size (D), lattice constant (a), cell volume (V), X-ray density (qx ray) and bulk density of $SrEr_xFe_{12-x}O_{19}$ (x =0.00, 0.01, 0.05 and 0.09)

Composition	Crystallite size (D) /nm	Lattice constant (a)/Å	Lattice constant (c)/Å	(c)/(a) Å	Cell volume (V)/Å^3	X-ray density (qx-ray)/g cm^{-3}
$SrFe_{12}O_{19}$	31.00	5.8794	22.358	3.9133	691.38	0.5107
$SrEr_{0.01}Fe_{11.99}O_{19}$	30.61	5.8814	23.0180	3.9161	691.38	0.5805
$SrEr_{0.05}Fe_{11.95}O_{19}$	30.40	5.8814	23.0180	3.9161	691.38	0.5769
$SrEr_{0.09}Fe_{11.91}O_{19}$	30.30	5.8814	23.0180	3.9161	691.38	0.5729

The unit V cell of the hexagonal system is determined by the relation V cell = 0.866 a^2c Where, a and c are lattice parameter obtained for the hexagonal system. From the XRD profile, an average size of nanoferrite crystallites was determined by Debye-Scherer equation (d) and is determined by the Scherrer's formula.

$$D = \frac{K\lambda}{\beta\cos\theta} \quad \text{..... (3)}$$

Where, K= 0.89 is a constant of Scherrer's value for the hexagonal system, λ = 0.15406 nm wavelength of the incident X-rays, β is the FWHM of diffraction peak, θ is the Bragg diffraction angle. The average value of crystallite size obtained was in the range 30-35 nm and values are tabulated in Table 1. Hypothetical X-ray thickness (dx) of each sample was determined using the formula [12]

$$Dx = \frac{ZM}{NV} \quad \text{..... (4)}$$

Where Z = 2, number of particles per unit cell, M is atomic weight, N is Avogadro's number and V is unit cell volume.

The cell volume of the $SrEr_xFe_{12-x}O_{19}$ patterns were set in the various boundaries a, c and V are tabulated in table 1. X-ray thickness is in the range 0.5107-0.5729 cm^{-1}. The decrease in the X-ray thickness was more because of doping of the larger molecular weight (104.116 amu) and

ion volume (0.1034 nm) of the Er^{3+}ion compared to the smaller molecular weight (87.62 amu) and largest ion radius (0.112nm) of strontium ions.

Magnetic properties

The effects of erbium doped strontium hexaferrites were analysed by vibrating sample magnetometer at room temperature operated at an applied magnetic field of 10 kOe. The magnetic parameters i.e., saturation magnetization (Ms), coercivity (Hc) and remnant magnetization (Mr) were determined based on these curves and the values are tabulated in table 2. The hysteresis curves of all samples of M- types hexaferrites with the formula, $SrErxFe_{12-x}O_{19}$ (x = 0.00, 0.01, 0.05 and 0.09). On the whole, the *M*s of these samples were more than 25 emu/g, which contained certain amount of $SrFe_{12}O_{19}$. Similarly, the Hc of the nanocomposites were more than 4500 G, the composites are in comparison to a conventional ferromagnetic and could be considered as hard-magnetic materials as shown in Fig. 3 [23].

The magnetic properties of substituted hexagonal ferrites are impacted by the electronic configuration of substituted or doped cations. The substituted Er^{3+} has an electronegativity of 1.17. The Fe^{3+} ion has five unpaired electrons and the hexagonal ferrites have a total of 12 Fe^{3+} occupied in five distinct sub-lattices. One is tetrahedral ($4f_1$), three are octahedral (12k, 2a and $4f_2$), and one is trigonal bipyramidal (2b). Of the twelve Fe^{3+} ions, four are oriented downwards, at $4f_1$ (2 Fe^{3+}) and eight $4f_2$ ($2Fe^{3+}$) are oriented upwards, at 12k (6 Fe^{3+}), 2a (1 Fe^{3+}) and 2b (1 Fe^{3+}). Thus, magnetic moment is caused by the remaining $4Fe^{3+}$ions, which have an upward orientation while the four downward and four upward spins cancel each other [24].

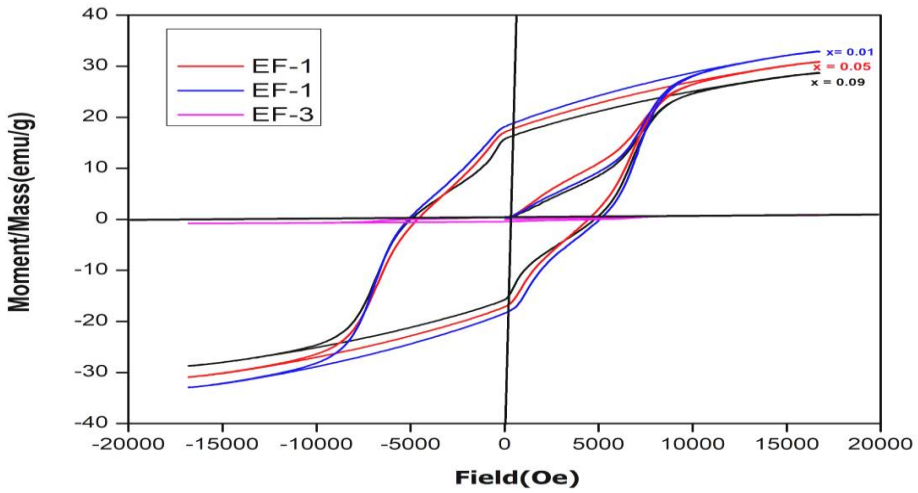

Fig. 3 Hysteresis curves of $SrEr_xFe_{12-x}O_{19}$ (FO; x=0.0, EF-1; x=0.01, EF-2; x=0.05 and EF-3; x=0.09)

Saturation magnetization (Ms) is reduced due to addition of Er^{3+} ions. The magnetic parameters were calculated using the following relationship

$$\eta\beta = \frac{M \, X \, Ms}{5585} \qquad \ldots\ldots\ldots (5) \qquad s = \frac{Mr}{Ms}$$

$$\ldots\ldots\ldots (6) \qquad K = \frac{Hc \, X \, Ms}{2a0.64}$$

$$\ldots\ldots\ldots (7)$$

Where $\eta\beta$ is the magnetic movement/ formula unit in μb, Ms - saturation magnetization (emu/g) Mr - remanence magnetization, M - molecular weight in g, 5585-magnetic factor, K-magnetic anisotropic constant and Hc- coercity.

Table.2 The values of saturation magnetization and their related data of synthesized nanoferrites (FO; x=0.0, EF-1; x=0.01, EF-2; x=0.05 and EF-3; x=0.09)

Name of composition	NPs symbol	Ms(emu/g)	Mr(emu/g)	Mr/Ms	Hc(Oe)	nβ(uβ)

$SrFe_{12}O_{19}$	EO	28.715	15.841	0.55166	4939.8	5.458
$SrEr_{0.01}Fe_{11.99}O_{19}$	EF1	30.909	17.113	0.55328	4537.70	6.734
$SrEr_{0.05}Fe_{11.95}O_{19}$	EF2	32.930	18.254	0.55432	5090.3	7.031
$SrEr_{0.09}Fe_{11.91}O_{19}$	EF3	34.824	19.318	0.55473	5232.5	7.536

A site substitution increases the magnetization. Hc magnetic moment of Fe^{3+} is higher than Er^{3+}. Therefore, the magnetization of B sub lattices increased as a result of an increase in Fe^{3+} ions at the B location [25]. Thus, lesser magnetic Er^{3+} replaced from the samples causes increase in magnetization. According to results, the saturation magnetization and remanence increases with increasing erbium doping. The rise in the Ms value when x exceeds 0.09. Nevertheless, a larger magnetism in the lattice is generated by an increase of hyperfine fields in the 12K and 2b sites as a result of the super exchange interaction in Fe^{3+}-O - Fe^{3+} [26]. Which affects Er^{3+} and the (host) Fe^{3+} ions respective ionic radii as well. The values of Ms and Mr with content are compared in supplementary figure S1. The table.2 show the values of saturation magnetization and related data.

Thermal analysis

The thermal degradation of $SrEr_{0.09}Fe_{11.91}O_{19}$ has been studied and two major weight loss have been observed and the graph is showed in supplementary file.S2. In the first step, loss of water molecules presents within the lattice occur at 100 ℃, and also decomposition of urea-nitrate occurred at 350 ℃ [27].

In the next step the weight loss associated with the decomposition of the residual organic material observed within the range of 350-580 ℃. Breakdown of metal hydroxide and development of hexagonal ferrite can be completely performed below 600 ℃. Above 600 °C, no noteworthy weight loss was observed, but the phase formation of ferrite crystals might have taken place [28-29]. Therefore, all the produced solids were calcinated around 1200°C for 4 h in high-temperature muffle furnace and exploited for intended investigations [30].

SEM Studies

The grain and morphology and particle size of synthesized $SrEr_xFe_{12-x}O_{19}$ (x = 0.00, 0.01, 0.05 and 0.09) depicted in fig. 4 (a-d). The figure showed that some have rod shape; some have hexagonal platelet like grain with particles are placed irregular manner. The particle sizes are calculated and they found to be in the range of 30-31 nm. The synthesized samples showed that the surfaces with agglomerated particles and magnetic interaction between individual particles could be the reason for the observed agglomeration which leads to the formation of large particles [31-32]. To examine the grain size, it was confirmed that as an increase in concentration by x moles, the grain size decreases. It has been reported that in auto-combustion technique using urea as a fuel the reaction involves crystallization.

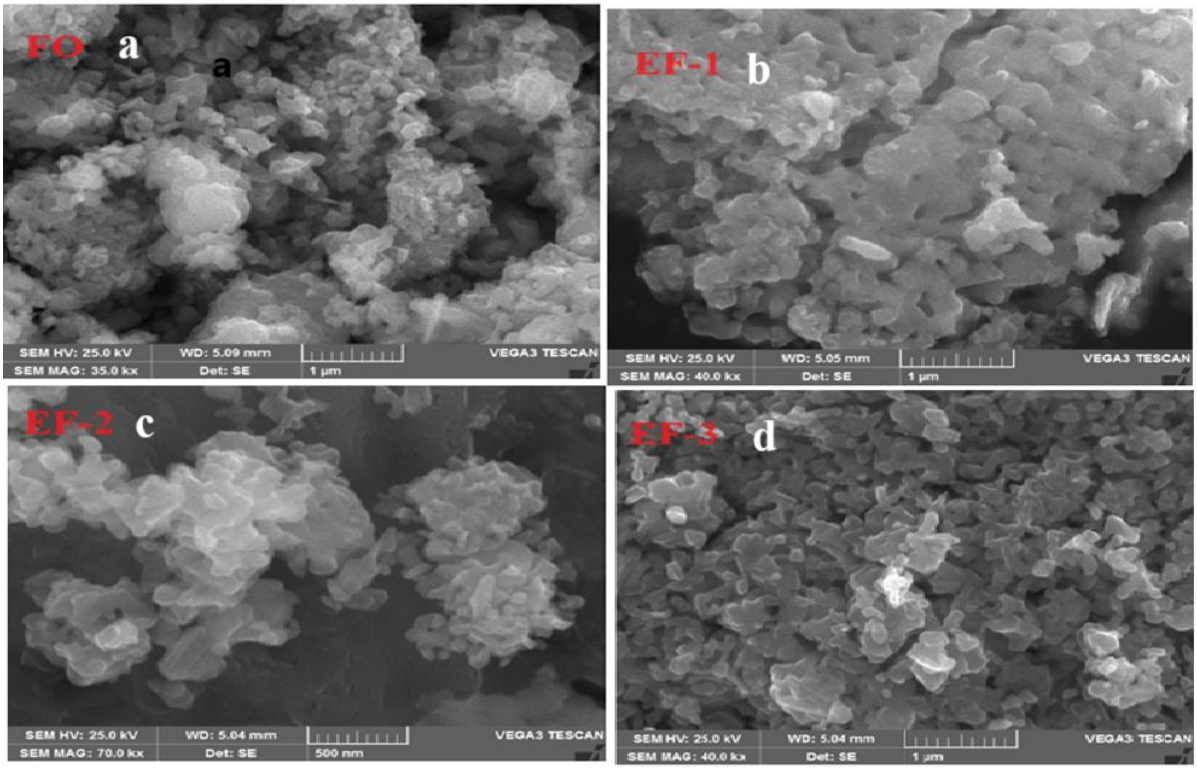

Fig.4 (a-d) SEM micrographs of M-type hexaferrites $SrEr_xFe_{12-x}O_{19}$ for all compositions FO; (a) x=0.00, EF-1; (b) x=0.01, EF-2; (c) x=0.05, EF-3 (d) x=0.09

The crystals obtained from a solution of nanoparticles to the M-HF's. This is due to short period of time reaction time and requirement of high temperature to complete the reaction [33].

EDX Studies

The percentage of each element in the synthesised $SrEr_xFe_{12-x}O_{19}$ nanoparticles with a temperature of 1200 ℃ and a time period of 3 h are recorded using energy dispersive X-ray analysis spectra EDS (Carl Zeiss, Model: EVOLS15, Germany). The spectra in figure 5 (a-d) shows the presence of elements, Sr, Er, Fe and O in expected values. The spectra present no impurity, indicating the high purity of all the samples and confirms high crystallinity of all the samples.

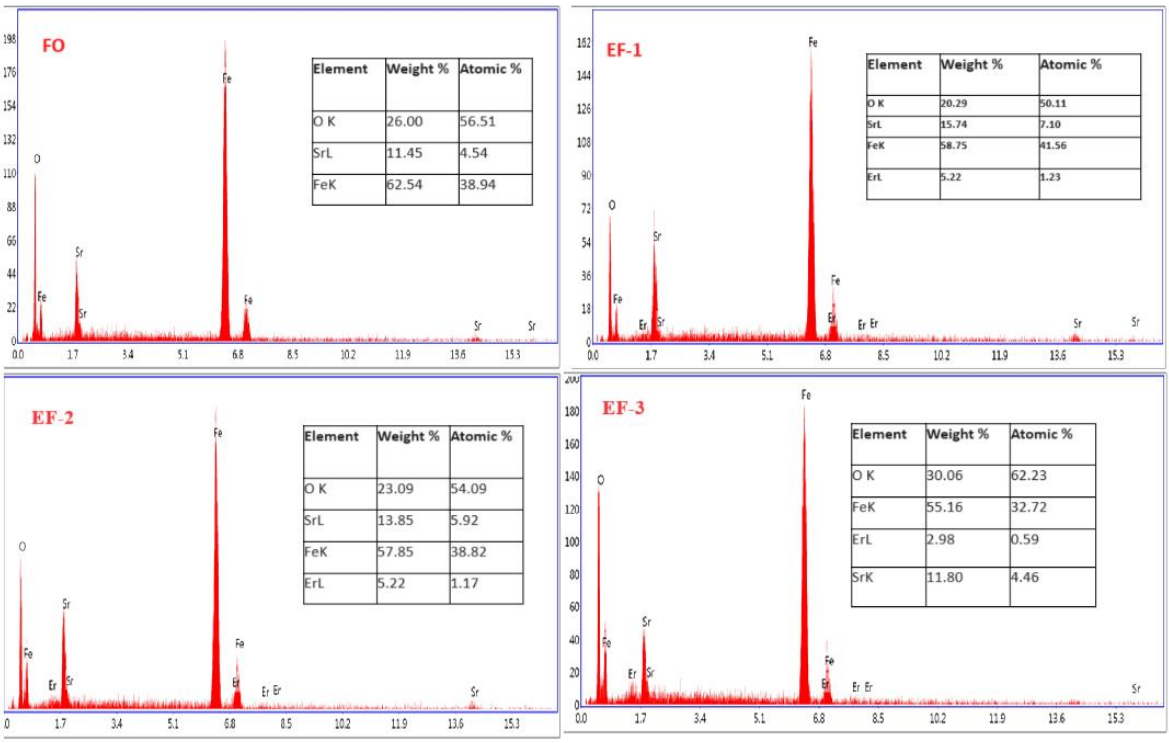

Fig.5: Elemental mapping and EDX spectrum of $SrFe_{12-x}Er_xO_{19}$ nanoparticles with a temperature of 900 ℃, (FO; x=0.0, EF-1; x=0.01, EF-2; x=0.05 and EF-3; x=0.09)

Optical properties

The UV-Visible spectra were recorded for all the $SrEr_xFe_{12-x}O_{19}$ nanoparticles using Shimadzu UV-2600 spectrophotometer and displayed an excitonic peak centre around 370 nm. The fundamental property of semiconductors is the band gap and is measured by UV-Visible

spectroscopy. The absorption in the visible region directly affects the colour of the chemicals which show transitions from the ground state to the excited state.UV-Visible spectra of bare strontium ferrite gave a band at 320 nm and erbium doped strontium ferrites at 370 nm. The band gap of $SrEr_xFe_{12-x}O_{19}$ was 2.5eV and the band gap of erbium doped magnetic nanoparticle increases from x=0.00 to x=0.09 with increasing concentration as calculated by the Tauc's relation. This showed that the band gap values increase as the particle size decreases. The band gap value of all NPs indicate that all the synthesized nanoparticle acts as semiconductors with band gap in the range 0-3 eV [34].

Absorption measured in the range of 200-800 nm. Using equation Kubelka-Munk (K-M) model to get optical reflection spectra and F(R) was calculated from the following conditions. All Er^{3+} doped nanoparticles were analysed to obtain the optical band gap.

$$Eg = \frac{hc}{\pi\lambda} = \frac{1240}{\lambda} \quad \text{……. (8)}$$

$$F(R\infty) = \frac{(1-R\infty)^2}{2R\infty} \quad \text{…….. (9)}$$

$$\{(F(R\ \infty)\ \ h\nu\}^{1/n}\ (h\nu\text{-}Eg) \quad \text{…….. (10)}$$

Where: h is the Planck is constant (6.626 x 10^{-34} Js), C-speed of light (2.99 x 10^8 ms^{-1}), λ - Wavelength of reflectance spectra, R∞ - Diffuse reflectance spectra, α -Absorption coefficient, ν -Frequency of the incident light, Eg –Band gap energy and n = 2 for direct band gap.

The absorption spectra of $SrEr_xFe_{12-x}O_{19}$ (x=0.00<x<0.09) recorded by preparing samples in polyaniline and showed two characteristic absorption peaks attributed to the synthesized $SrEr_xFe_{12-x}O_{19}$, one is around 285 nm and other is at 385 nm. The first absorption band assigned at around 300 nm is due to the π-π* electronic transitions and other is assigned at 385 nm. The absorption increases with increasing Er^{3+} concentration of $SrEr_xFe_{12-x}O_{19}$. In

accordance with Beer's law, the absorption is proportional to the number of absorbing molecules. These results suggest that there are interactions among $SrEr_xFe_{12-x}O_{19}$ nanoparticles as described by equations 10.

Photocatalytic studies

Photocatalytic degradation for four dyes such as Erichrome black-T (EBT), methyl Orange (MO) Methyl blue (MB) and 4-nitroaniline (4NA) were studied under UV light illumination using $SrEr_xFe_{12-x}O_{19}$. The probable mechanism of photo degradation is represented in the following reaction mechanism.

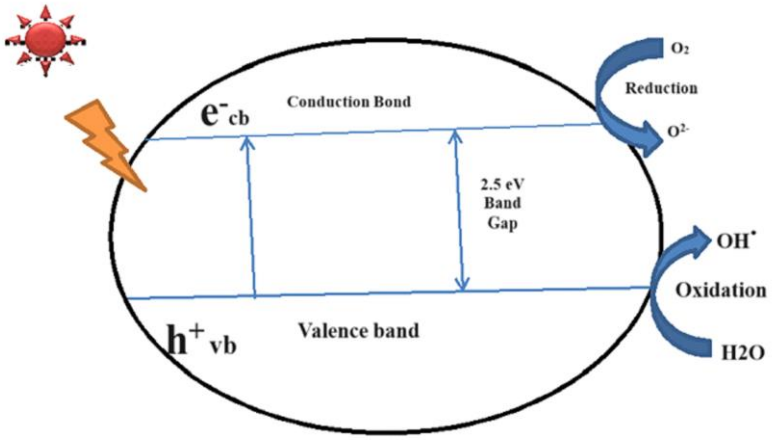

Fig. 6 Scheme of Mechanism of dye degradation in the presence of $SrEr_{0.09}Fe_{11.91}O_{19}$ under UV light

$SrFe_{12-x}Er_xO_{19} + h\nu\ (vis) \longrightarrow SrFe_{12-x}Er_xO_{19}\ (e^-CB + h^+VB)$ ……. (11)

$SrFe_{12-x}Er_xO_{19}\ (e^-CB) + O_2 \longrightarrow O_2^{\cdot}$ ..... (12)

$O_2^{\cdot} + h^+ \longleftrightarrow HOO^{\cdot}$ ..…… (13)

$2HOO^{\cdot} \longrightarrow H_2O_2 + O_2$ ..……. (14)

$SrFe_{12-x}Er_xO_{19}\ (h^+VB) + H_2O \longrightarrow HO^{\cdot} + H^+$ …...…… (15)

Dye + $HO^{\cdot}$ + $O_2^{\cdot}$ ⟶ CO_2 +H_2O (By product) ..…….. (16)

Dye + $SrFe_{12-x}Er_xO_{19}$ ⟶ (h^+VB) Oxidation Product ……..…….. (17)

Dye + $SrFe_{12-x}Er_xO_{19}$ ⟶ (e^-CB) Reduction Product …… (18)

Among the products, hydroxyl radicals (•OH) are the most significant contributors in dye degradation. Figure 6 depicts a schematic illustration of dye photodegradation utilizing $SrEr_xFe_{12-x}O_{19}$ under UV light. The photodegradation was initiated only when the $SrEr_xFe_{12-x}O_{19}$ photocatalyst interacted with the UV light. During the photoexcitation, electrons in the conduction band (CB) and holes in the valence band (VB) are arranged. The photogenerated electrons in the CB react with molecular oxygen to produce anionic superoxide radical (•O_2) through reduction [35]. e^- attracts to the photogenerated hole in VB by hydroxyl ions or water molecule to produce the most reactive hydroxyl radical (•OH) over oxidation [36]. The H_2O_2 produced due to the superoxide anion radical's interact with e^- /h+ pairs. On the $SrEr_xFe_{12-x}O_{19}$ surface, the organic molecules are attacked by these effective species which act as strong oxidizing agents. As a result, these organic dye molecules easily attacked by ions leads to by-products [37]. This is known as the redox reaction, which occurs on the photocatalyst's surface. Fig.8 showed the comparison of photodegradation studies of $SrEr_xFe_{12-x}O_{19}$ against EBT, MO, MB and 4NA as a targeted pollutant under UV light illumination. UV-Visible spectroscopy was employed to record the decolourisation.

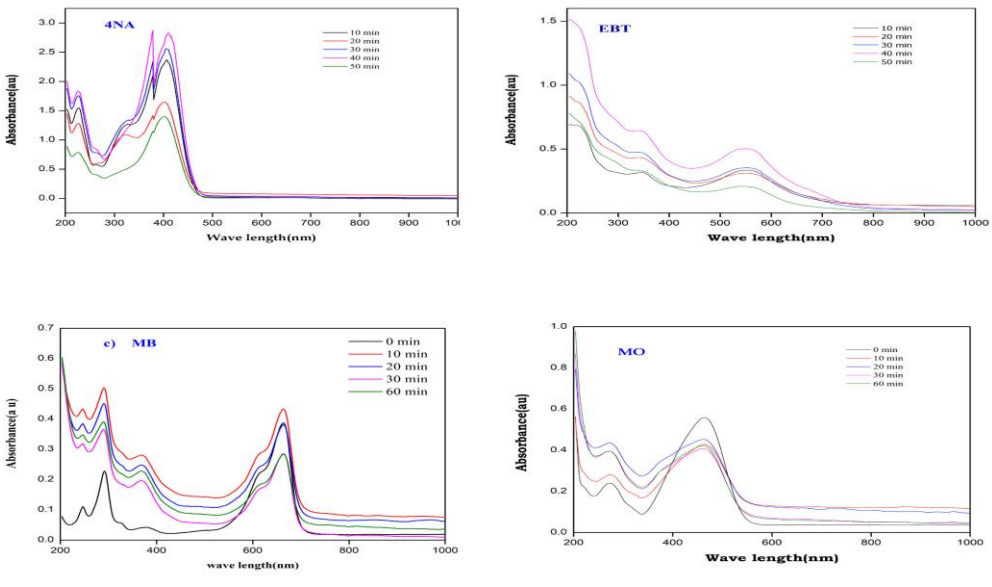

Fig. 7 Band gap energy of different time interval in the presence of $SrEr_{0.09}Fe_{11.91}O_{19}$

of EBT, MO, MB and 4NA dyes over $SrFe_{12-x}Sm_xO_{19}$. Initially, no changes were observed but after irradiation, it was discovered that the dye degrades. The evaluation of degradation efficiency of $SrEr_xFe_{12-x}O_{19}$ on 4NA, EBT, MB and MO dyes was carried out. In presence of Sr $Er_{0.09}Fe_{11.91}O_{19}$, 98 % degradation of 4NA dye has occurred in 90 min. while EBT, MB and MO dyes degraded to 87, 72 and 78% respectively in 90 min. 4NA dye showed excellent degradation when compared to other dyes and the results are showed in supplementary table S-5. Based on the results only 4NA dye was considered for further studies. In continuation, the photodegradation of 4NA was conducted at different parameters like, concentrations of dye, various amount of catalyst at different pH conditions etc., The plots in Fig. 7 show the effect of concentration and the catalyst load on the degradation of dye.

Table.3 Comparison table: Time of degradation and % of degradation of different dyes in the presence $SrEr_xFe_{12-x}O_{19}$ (x =0.00, 0.01, 0.05 and 0.09)

Samples	Time (Min)	% Degradation of dye			
		4NA	EBT	MO	MB
X=0.00	0	0	0	0	0
X=0.01	30	18	14	15	12
X=005	60	73	48	44	41
X=0.09	90	98	85	80	75

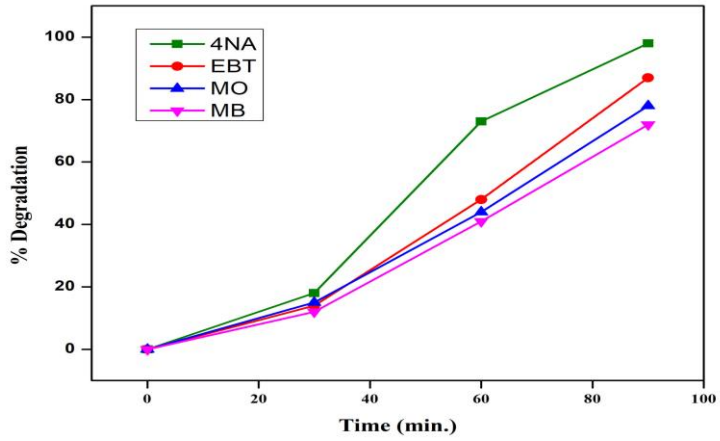

Fig. 8 Comparison of % degradation of different dyes in the presence of Sr $Er_{0.09}Fe_{11.91}O_{19}$

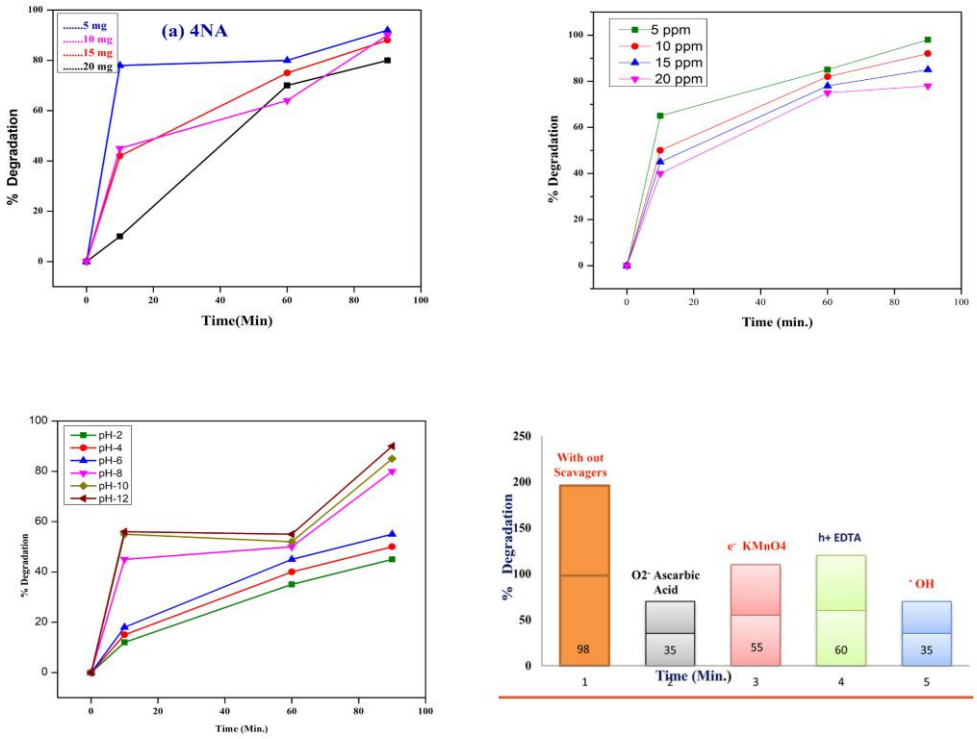

Fig. 9. Photocatalytic activity of $SrEr_xFe_{12-x}O_{19}$ (a) Effect of concentration (b) Effect of catalytic load (c) Effect of pH (d) Effect of different scavengers during the degradation of 4NA dye.

Effect of dye concentration

Dye degradation ability of synthesized nano materials have been determined by taking 4-nitro aniline (4-NA), EBT, MO and MB. Among them 4-NA found to have degraded effectively in lesser time. Therefore, the degradation of 4NA in different concentration was studied by taking dye from 5 to 20 ppm, with a catalyst dosage of 20 mg per 100 mL, as illustrated in Figure 9(a). The highest degradation of 4NA dye was appeared at a concentration of 5 ppm [38]. As the concentration of dye increases, the number of dye molecules adsorbed on the surface of the catalyst increases and reduces the active sites available for catalytic reaction and hence the degradation rate decreases.

Effect of catalyst dosage

The efficiency of the $SrFe_{12-x}Er_xO_{19}$ catalyst at an optimal load was determined by varying the catalyst amount from 5 to 20 mg per 100 mL and by adding 5 ppm 4NA dye. The highest percentage of degradation attained for the 15 mg of the catalyst load as showed in Figure 9(b) [39]. Hence, 15 mg catalyst weight was chosen for the further photocatalytic experiments.

Effect of pH

One of the main parameters influencing the photocatalytic polluted water treatment is the pH. To obtain maximum degradation efficiency, pH must be optimised. The pH of the dye solution was varied from 2 to 12 to investigate the influence of pH on dye degradation and the results were shown in Figure 9(c). The results reveal that at lower pH, the proportion of dye degradation was less. Therefore, the increased photocatalytic degradation raises the pH of the dye solution, which may be due to availability of more number of •OH in alkaline medium and will create an additional OH radicals by interacting with holes produced by the catalyst electronic excitation [40].

Electronic properties

On the other hand, the density of states (DOS) of $SrEr_xFe_{12-x}O_{19}$, where Er^{3+}occupy the 12k site, displays a creation of low-lying energy occupied bands in the majority spin channel

extending from 4.4 to 1.9 eV, in addition to a narrow band in the minority spin channel, decreasing the band gap energy to 1.01 eV. These bands are characteristic of the electronic configuration A2, 2g, T5, 2g, T3, 1g of the octahedral coordinated Er^{3+}.

This study suggests that the band gap would be decreased upon doping with Er^{3+} and Fe^{3+} ions. However, as it is seen in Section Photocatalytic studies, the experimental band gap energy from the present work is not affected upon doping. It is measured to be 2.5 eV for the SrM compound. Response, making this material very interesting for polluted water treatment applications [41].

Recycling of catalyst

A catalyst recycling experiment was utilized to evaluate the photocatalyst's stability throughout the degradation process. 50 mg of 4NA catalyst in 100mL solution of 10 ppm and exposed to sunlight source. Reuse efficiency of catalysts was done by further processing of the catalyst after collecting it from the first cycle of catalyst activity. The degradation efficiency and decomposition potency of $SrEr_xFe_{12-x}O_{19}$ and 4NA dye was almost identical for 2 cycles. In the second cycle, the catalytic activity decreased by 10% in 60 min. It was observed that 80% of dye degradation was achieved in 45 min, when it was used in the third cycle. The photocatalyst could be used for three cycles with minimal change in catalyst property and degradability [42].

Conclusion

Erbium doped strontium M-type hexagonal ferrites $SrEr_xFe_{12-x}O_{19}$ (x=0.0, 0.01, 0.05 and 0.09) nanoparticles have been synthesized through auto-combustion method using urea as fuel. The XRD investigation revealed the existence of crystalline and hexagonal structure with absence of Er_3O_3 as separate phase. SEM studies for erbium doped ferrites indicated the platelets like grains with well-defined hexagonal shape. FTIR analysis for pure and doped strontium ferrite samples show that Fe^{2+}/Fe at 454 cm^{-1}, Fe-O stretching modes appeared at 591 cm^{-1}. Hysteresis curves from VSM analysis at room temperature exhibited ferromagnetism

behaviour for x=0.01 to 0.09. Coercivity found to be more than 4.9 kOe. As erbium substitution increases, Hc and Mr values decreases which confirm hard magnetization. Photo-degradation ability of $SrEr_{0.09}Fe_{11.91}O_{19}$ on EBT, MO, MB and 4-NA dyes determined. All dyes degraded but 4-NA degraded to 98%. The degradation efficiency of 4NA compared with the literature values. The band gap energy (Eg) of 2.5 eV, indicated that this $SrEr_xFe_{12-x}O_{19}$ compound could be used in permanent magnets and also polluted water treatment.

Acknowledgements

This work is supported by Department of Chemistry, Sahyadri Science College, Shivamogga, for providing experimental facilities and also instrumentation facility. Authors also extend thanks to USIC, University of Guwahati, Assam for providing the VSM spectral data and SAIF, Karnataka University, Dharwad for providing Thermogravimetric analysis.

Conflict of Interests

The authors declare no conflict of interest.

Fundings

There is no funding.

References

1. Nag.S, Roychowdhury.A, Das.D, Das. S, Mukherjee.S, Structural and magnetic properties of erbium (Er^{3+}) doped nickel zinc ferrite prepared by sol-gel auto-combustion method, J. Magn. Magn. Mater. 466 (2018) 172-179. https://doi.org/10.1016/j.jmmm.2018.06.084
2. Imtisal Ayman, Muhammad Aadil, Basem Al Alwan, Habib Khemira, Sonia Zulfiqar, Awais Khalid, Zaid. M, Aldhafeeri, Muhammad Farooq Warsi, Surfactant-mediated wet-chemical synthesis of magnetically retrievable and structurally tuned cobalt ferrite: A visible light-triggered photocatalyst for the abatement of azo dye,Inorganic Chemistry Communications, 174, 1,2025,113988, https://doi.org/10.1016/j.inoche.2025.1139884.

3. Eman. A, Al-Abbad, Muhammad Aadil, Moutaz Aldrdery, Noura Dawas Alkhaldi, Awais Khalid, Mazen R. Alrahili, Meri Algarni, Atef El Jery, Mohamed R. El-Aassar, Nanostructured codoped neodymium orthoferrite synthesized via the hydrothermal route for photocatalytic annihilation of crystal violet dye,Ceramics International,50, 24,2024,54943-54954 https://doi.org/10.1016/j.ceramint.2024.10.343.

4. Rehman, M. Rukh, Akram, M. Aftab, Gul, I. Hussain, Improved Electrical Properties of Strontium Hexaferrite Nanoparticles by Co^{2+} Substitutions. JACS Omega, 7 (2022) 48. https://doi.org/10.1021/acsomega.2c03256

5. Davar.F, M. Salavati-Niasari, Synthesis and characterization of spinel-type zinc aluminate nanoparticles by a modified sol–gel method using new precursor, J. Alloy. Compd. 509 (5) (2011) 2487–2492. https://doi.org/10.1016/j.jallcom.2010.11.058

6. Kaur.P, Chawla.S.K, Narang.S.B, Pubby.K, Structural, magnetic and microwave absorption behavior of Co-Zr substituted strontium hexaferrites prepared using tartaric acid fuel for electromagnetic interference suppression, J. Magn. Magn. Mater. 422 (2017) 304–314.http://dx.doi.org/10.1016/j.jmmm.2016.11.054

7. Buzinaro.M.A.P, Ferreira.N.S, Cunha.F, Macedo.M.A, The effect of different alkali metal chloride fluxes on the phase formation and properties of Sr-based hexaferrite, $SrFe_{12}O_{19}$ materials. Ceram. Int. 5 (2015) 42.http://dx.doi:10.1007/s10854-017-6999-y

8. Lakshmikantha.J, Krishnamurthy.G, Nagabhushan.B.M, Naveen.C.S. and Melagiriyappa.E, Effect of Ce^{3+} Substitution on Sr^{2+}; Structural and Magnetic Properties of Nanocrystalline $SrFe_{12}O_{19}$ Hexaferrites Prepared by Self-Propagation Method Using Mixed Fuels. J. Supercond. Nov. Magn. 35 (2022) 2485-2492. http://dx.doi.org/10.1007/s10948-022-06223-7

9. Ramírez-Ayala.M.F, Pérez-Juache.T.j, Herrera-González.A.M, Lobo Guerrero.A, "Effect of the neodymium doping on the magnetic and structural properties of the Sr-hexaferrite obtained by the Pechini method." Superficies Vacío, 35 (2022) 221201.

https://doi.org/10.47566/2022_syv35_1-221201

10. Lakshmikantha.J, Krishnamurthy.G, Nagabhushan., E. Melagiriyappa, J. Solid State Chem. 315 (2022) 123465. https://doi.org/10.1016/j.jssc.2022.123465

11. Lakshmikantha.J, Krishnamurthy.G, Nagabhushan.B.M, Melagiriyappa.E, Dielectric properties and magnetic behavior of Gd^{3+} substituted M-type $SrFe_{12}O_{19}$ nanoferrites by auto combustion method using urea and citric acid mixtures as a dual fuel. J. of Solid State Chemistry. 315 (2022) 123465. https://doi.org/10.1016/j.jssc.2022.123465

12. Zulfiqar Ali, Muhammad Aadil, Breeha zainab, MuhammadHassan Rasool, Warda Hass an, Shamroza Mubarik, Zubair Ahmad, Nada A. Almuhous, AsmaA Alothman, Munawar Hussain, Synthesis of nanostructured In_2O_3 ceramics via a green and chemical method for the mineralization of crystal violet dye: A comparative study, Inorganic ChemistryCommunications,157,2023,111399 https://doi.org/10.1016/j.inoche.2023.111399.

13. Bishoge.O.K, ZhangL, S.L. Suntu, Jin.H, Zewde.A. A, Qi.Z, Remediation of water and waste water by using engineered nanomaterials: a review, J. Environ. Sci. Health Part A. 53 (2018) 537–554. https://doi.org/10.1080/10934529.2018.1424991

14. Deng.W, Zhao.H, Pan.F, Feng.X, Jung.B, Abdel-Wahab.A, Batchelor.B, Li.Y, Visible-light-driven photocatalytic degradation of organic water pollutants promoted by sulfite addition, Environ.Sci.Technol.51 (2017) 13372–13379. http://dx.doi.org/10.1021/acs.est.7b06200

15. M.A. Mahadik, S.S. Shinde, S.S. Kumbhar, H.M. Pathan, K.Y. Rajpure, C.H. Bhosale, Enhanced photocatalytic activity of sprayed Au doped ferric oxide thin films for salicylic acid degradation in aqueous medium, Journal of Photochemistry and Photobiology B: Biology, 142 (2015) 43-50. https://doi.org/10.1016/j.jphotobiol.2014.09.021

16. Thippeswamy.A, Manjunatha.M.N, Chavan, Prabhakar, Krishnamurthy.G. “Synthesis,

Structural, Magnetic, and Electrochemical Properties of Er-Ni Doped Strontium Nanoferrites, J. Anal. Bioanal. Electrochem., 16 (2024), 1026-1045. https://www.doi.org/10.22034/abec.2024.718628.

17. Lakshmikantha.J. Krishnamurthy.G, Nagabhushan.B.M, Melagiriyappa.E, Dielectric properties and magnetic behavior of Gd^{3+} substituted M-type $SrFe_{12}O_{19}$ nanoferrites by auto combustion method using urea and citric acid mixtures as a dual fuel. J. of Solid State Chemistry. 315 (2022) 123465. https://doi.org/10.1016/j.jssc.2022.123465
18. Mahapatro.J, Agrawal.S, Influence of erbium substitution on structural, optical and dielectric properties of strontium hexaferrite. Bull Mater Sci. 47 (2024) 26. https://doi.org/10.1007/s12034-023-03093-0.
19. Sun, E. Zhu, Q, Rehman.H.U, Wu.T, Cao.X. Wang.N, Magnetic Material in Triboelectric Nanogenerators: A Review. Nanomaterials, 14, (2024) 826. https://doi.org/10.3390/nano14100826.
20. Almessiere.M.A, Slimani.Y, El.H.S, Sayed.A. Bayka.I. Ercan, Microstructural and magnetic investigation of vanadium-substituted Sr-nanohexaferrite. J. Magn. Magn. Mater. 471 (2019) 124-132. https://doi:10.1016/j.jmmm.2018.09.054.
21. Ashiq.M. N, Iqbal.M. J, Gul.I. H, Structural, magnetic and dielectric properties of Zr–Cd substituted strontium hexaferrite ($SrFe_{12}O_{19}$) nanoparticles, J. Alloys Compd. 487 (2009) 341–345. https://doi.org/10.1016/j.jallcom.2009.07.140.
22. Ugur Topal, Husnu Ozkan, Huseyin Sozeri, Synthesis and characterization of nanocrystalline $BaFe_{12}O_{19}$ obtained at 850°C by using ammonium nitrate melt, J. Magn. Magn. Mater.284, (2004) 416-422. https://doi.org/10.1016/j.jmmm.2004.07.009.
23. Asha D. Patil, Ram. A. Pawar, Sunil. M. Patange, Santosh. S. Jadhav, Shyam K. Gore, Sagar E. Shirsath, and Sher Singh Meena, TiO_2-Doped $Ni_{0.4}Cu_{0.3}Zn_{0.3}Fe_2O_4$ Nanoparticles for Enhanced Structural and Magnetic Properties.

ACS Omega, 6(28), (2021) 17931-17940. https://doi. 10.1021/acsomega.1c01548.

24. Slimani.Y, Güngünes.H, Nawaz.M, Manikandan.A., El Sayed.H.S, Almessiere.M.A, Sözeri.H, Shirsath.S.E, Ercan.I, Baykal.A, Magneto-optical and microstructural properties of spinel cubic copper ferrites with Li-Al co-substitution, Ceramics International, 44(12) (2018) 14242-14250. https://doi.org/10.1016/j.ceramint.2018.05.028.

25. Mah Rukh Rehman, Muhammad Aftab Akram, Iftikhar Hussain Gul, Improved Electrical Properties of Strontium Hexaferrite Nanoparticles by Co^{2+} Substitutions, ACS Omega 7 (48) (2022) 43432–43439 https://doi. 10.1021/acsomega.2c03256.

26. Cui, Caixi, "Structural and Magnetic Properties of Sm-Doped Strontium Hexaferrite ($SrFe_{12-x}Sm_xO_{19}$) Powders. Materials Focus 3 (5) (2014) 355-360. http://dx.doi.org/10.1080/10667857.2018.1465746.

27. Mahadule.R.K, Arjunwadkar.P.R, Mahabole.M.P, Synthesis and Characterization of $Ca_xSrBa_{1-x-y}Fe_{12-x}LaO_{19}$ by Standard Ceramic Method, (2013) 198970. http://dx.doi.org/10.1155/2013/198970.

28. Sankaranarayanan.V. K.and Khan.D. C, "Mechanism of the Formation of Nanoscale M-Type Barium Hexaferrite in the Citrate Precursor Method," J.Magn. Magn. Mater., 153(3) (1996) 337-346. http://dx.doi 10.1016/0304-8853(95)00537-4.

29. Robert C. Pullar, Hexagonal ferrites: A review of the synthesis, properties and applications of hexaferrite ceramics, Progress in Materials Science, 57(7) (2012) 1191-1334. https://doi.org/10.1016/j.pmatsci.2012.04.001S.K

30. Chawla.S.K, Mudsainiyan.R.K, Meena.S.S, Yusuf.S.M, "Sol–gel synthesis, structural and magnetic properties of nanoscale M-type barium hexaferrites $BaCoxZrxFe_{12-x}O_{19}$ J. Magn. Magn. Mater. 350 (2013) 23–29 https://doi.org/10.1016/j.jmmm.2013.09.007.

31. Srivastava.D, Lee.I, Nanorice and Nanospears from Polymer Nanospheres. Advanced materials, 18(18) (2006) 2471–2475. https://doi.org/10.1002/adma.200601123

32. Mane.D. R, Birajdar, Patil.D.D, Redistribution of cations and enhancement in magnetic properties of sol–gel synthesized $Cu_{0.7-x}$ Co x $Zn_{0.3}Fe_2O_4$ ($0 \leq x \leq 0.5$). J Sol-Gel Sci. Technol. 58 (2011) 70–79 https://doi.org/10.1007/s10971-010-2357-8.

33. Asiri.S, Güner.S, Korkmaz.A.D, Md. Amir, Batoo.K.M, Almessiere.M.A, Gungunes.H, Sözeri.H, Baykal.A, Magneto-optical properties of $BaCryFe_{12-y}O_{19}$ ($0.0 \leq y \leq 1.0$) hexaferrites, J. Magn. Magn. Mater. 451 (2018) 463-472. https://doi.org/10.1016/j.jmmm.2017.11.100K.

34. Harish.K.N, BhojyaNaik.H.S, Prashanth kumar.P.N, Viswanath.R, Synthesis, enhanced optical and photocatalytic study of Cd–Zn ferrites under sunlight. Catal. Sci. Technol., 2 (2012) 1033–1039 https://doi. 10.1039/c2cy00503dS.

35. Gul.S, Yousuf.M.A, Anwar.A, Warsi.M.F, Agboola.P.O, Shakir.I, Shahid.M, Al-substituted zinc spinel ferrite nanoparticles: Preparation and evaluation of structural, electrical, magnetic and photocatalytic properties, Ceramics International 46 (2020) 14195. https:// doi.org/10.1016/j.ceramint.2020.02.228.

36. Anpo.M, Costentin.G, Giamello.E, Lauron-Pernot.H, Sojka.Z, Characterisation and reactivity of oxygen species at the surface of metal oxides, J. Catal. 393 (2021) 259–280. https://doi.org/10.1016/j.jcat.2020.10.011.

37. Sathisha.H.C, Anitha, Krishnamurthy.G, Malathesh Pari, Soundarya.T.L, Nagaraju.G, Synthesis and characterization of CuO-NiO nanocomposite for dye degradation and electrochemical sensing of dopamine. Chemical Data Collections 48 (2023) 10108. https://doi.org/10.1016/j.cdc.2023.101081.

38. Sree.G.V, Nagaraaj.P, Kalanidhi.K, Aswathy.C.A, Rajasekaran.P, Calcium oxide a sustainable photocatalyst derived from eggshell for efficient photodegradationof organic pollutants, J. Clean. Prod. 270 (2020) 122294.

https://doi.org/10.1016/j.jclepro.2020.122294.

39. Sumantha.H.S, Rajagopal.S, Nagaraju.G, Shashank.M, Suresha.B.L, Facile and eco-friendly combustion synthesis of NiO particles for Photodegradation studies, Chem. Phys. Lett. 779 (2021) 138837. https://doi.org/10.1016/j.cplett.2021.138837.

40. Wang.D, Mueses.M.A, Angel.J, Marque.C, Machuca-Martínez.F, Grcic.I, Moreira.R.P.M, Puma.G.L, "Engineering and modeling perspectives on photocatalytic reactors for water treatment", Water Res. 202 (2021) 117421. https://doi.org/10.1016/j.watres.2021.117421.

41. Elansary.M, Belaiche.M, Ahmani Ferdi.C, Iffer.E, Bsoul.I, New nanosized Gd–Ho–Sm doped M-type strontium hexaferrite for water treatment application: experimental and theoretical investigations, RSC Adv. 10 (2020) 25239–25259. https://doi.org/10.1039/D0RA04722H

42. Sumadevi.R, Krishnamurthy.G, Prabhaker Walmik, Priya Rani.R. S, Satish Naik, Bhojya Naik.H. S, Nagaraja Naik, "Photocatalytic degradation of Eriochrome black-T and Evan's blue dyes under the visible light using PVA capped and uncapped Ag doped ZnS nanoparticles", Emergent Mater. 4 (2021) 447–456. https://doi.org/10.1007/s42247-020-00153-7.